Journal of Controlled Release 244 (2016) 257–268

Contents lists available at ScienceDirect

Journal of Controlled Release

journal homepage: www.elsevier.com/locate/jconrel

Tumor stroma-containing 3D spheroid arrays: A tool to study nanoparticle penetration

Dwi L. Priwitaningrum [a], Jean-Baptiste G. Blondé [b], Adithya Sridhar [b], Joop van Baarlen [c], Wim E. Hennink [d], Gert Storm [a,d], Séverine Le Gac [b], Jai Prakash [a,*]

[a] Targeted Therapeutics, Department of Biomaterials Science and Technology, MIRA Institute, University of Twente, Enschede, The Netherlands
[b] Applied Microfluidics for BioEngineering Research, MIRA Institute, University of Twente, Enschede, The Netherlands
[c] Laboratorium Pathologie Oost-Nederland (LabPON), Hengelo, The Netherlands
[d] Department of Pharmaceutics, Utrecht University, Utrecht, The Netherlands

ARTICLE INFO

Article history:
Received 22 June 2016
Received in revised form 5 September 2016
Accepted 7 September 2016
Available online 9 September 2016

Keywords:
Nanoparticles
3D *in vitro* model
Tumor penetration
Tumor stroma

ABSTRACT

Nanoparticle penetration through tumor tissue after extravasation is considered as a key issue for tumor distribution and therapeutic effects. Most tumors possess abundant stroma, a fibrotic tissue composed of cancer-associated fibroblasts (CAFs) and extracellular matrix (ECM), which acts as a barrier for nanoparticle penetration. There is however a lack of suitable *in vitro* systems to study the tumor stroma penetration of nanoparticles. In the present study, we developed and thoroughly characterized a 3D co-culture spheroidal array to mimic tumor stroma and investigated the penetration of silica and PLGA nanoparticles in these spheroids. First, we examined human breast tumor patient biopsies to characterize the content and organization of stroma and found a high expression of alpha-smooth muscle actin (α-SMA; 40% positive area) and collagen-1 (50% positive area). Next, we prepared homospheroids of 4T1 mouse breast cancer cells or 3T3 mouse fibroblasts alone as well as heterospheroids combining 3T3 and 4T1 cells in different ratios (1:1 and 5:1) using a microwell array platform. Confocal live imaging revealed that fibroblasts distributed and reorganized within 48 h in heterospheroids. Furthermore, immunohistochemical staining and gene expression analysis showed a proportional increase of α-SMA and collagen in heterospheroids with higher fibroblast ratios attaining 35% and 45% positive area at 5:1 (3T3:4T1) ratio, in a good match with the clinical breast tumor stroma. Subsequently, we studied the penetration of high and low negatively charged fluorescent silica nanoparticles (30 nm; red and 100 or 70 nm; green; zeta potential: −40 mV and −20 mV) and as well as Cy5-conjugated pegylated PLGA nanoparticles (200 nm, −7 mV) in both homo- and heterospheroid models. Fluorescent microscopy on spheroid cryosections after incubation with silica nanoparticles showed that 4T1 homospheroids allowed a high penetration of about 75–80% within 24 h, with higher penetration in case of the 30 nm nanoparticles. In contrast, spheroids with increasing fibroblast amounts significantly inhibited NP penetration. Silica nanoparticles with a less negative zeta potential exhibited lesser penetration compared to highly negative charged nanoparticles. Subsequently, similar experiments were conducted using Cy5-conjugated pegylated PLGA nanoparticles and confocal laser scanning microscopy; an increased nanoparticle penetration was found in 4T1 homospheroids until 48 h, but significantly lower penetration in heterospheroids. Furthermore, we also developed human homospheroids (MDA-MB-231 or Panc-1 tumor cells) and heterospheroids (MDA-MB-231/BJ-hTert and Panc-1/pancreatic stellate cells) and performed silica nanoparticle (30 and 100 nm) penetration studies. As a result, heterospheroids had significantly a lesser penetration of the nanoparticles compared to homospheroids. In conclusion, our data demonstrate that tumor stroma acts as a strong barrier for nanoparticle penetration. The 30-nm nanoparticles with low zeta potential favor deeper penetration. Furthermore, the herein proposed 3D co-culture platform that mimics the tumor stroma, is ideally suited to systematically investigate the factors influencing the penetration characteristics of newly developed nanomedicines to allow the design of nanoparticles with optimal penetration characteristics.

1. Introduction

Nanomedicines are designed to target anti-cancer agents to the dynamic tumor microenvironment sparing healthy tissues from severe side effects and thereby enhancing therapeutic index of anti-cancer

* Corresponding author at: Targeted Therapeutics, Department of Biomaterials Science and Technology, MIRA Institute for Biomedical Technology and Technical Medicine, University of Twente, Enschede, The Netherlands.
E-mail address: j.prakash@utwente.nl (J. Prakash).

http://dx.doi.org/10.1016/j.jconrel.2016.09.004
0168-3659/

therapies. Nanoparticles extravasate into tumors through leaky and tortuous blood vasculature and are retained intratumorally for prolonged periods as the lymphatic system is absent or only poorly developed, a phenomenon referred to as Enhanced Permeability and Retention (EPR) effect [1–5]. The physicochemical properties of nanoparticles such as size, shape, charge, and the nature of material they are made of play a major role in determining their fate in the body as well as within tumors [6–9]. Despite an overwhelming therapeutic success of nanomedicines in preclinical tumor models, only a limited therapeutic benefit has been achieved in the clinical situation. One major concern in the clinic is the limited penetration of nanoparticles into tumors [10,11]. In contrast to commonly used preclinical subcutaneous tumor models, clinical tumors are highly different due to the presence of fibrotic tumor stroma [12]. Recent studies have acknowledged that penetration of nanoparticles in the target tissue and their accumulation at the tumor site is affected by many factors such as the characteristics of nanoparticles (size, charge, and shape), as well as the tumor microenvironment and intracellular signaling networks [13–16].

Evidence is increasing that tumor growth is not solely dependent on cumulative gene mutations, but also significantly influenced by the surrounding tumor stroma [17]. Specifically, cancer cells co-exist in the tumor microenvironment with stromal components which is mostly comprised of fibroblasts, endothelial cells, inflammatory immune cells, adipocytes, and extracellular matrix (ECM) [18]. Complex interactions between tumor cells and the stroma govern tumorigenesis, tumor progression, and metastasis. Fibroblasts, as the most abundant component in certain tumor types such as breast and pancreas cancer, are protumorigenic, and can transform into cancer associated-fibroblasts (CAFs) [17,19]. CAFs secrete an enormous amount of ECM which develops fibrotic tissue within the tumor stroma. Furthermore, CAFs provide resistance to tumor cells by secreting growth factors, which ultimately leads to treatment failure [17,19]. Thus, reflecting these key-characteristics of the tumor stroma in an *in vitro* culture model is of high interest for drug and/or nanomedicine screening.

Three-dimensional (3D) culture models such as spheroids better resemble the *in vivo* situation compared to 2D models, and more realistically recapitulate the tumor microenvironment offering advantages of resembling *in vivo* tumor microenvironment, enabling thereby a better understanding of molecular and cellular mechanisms [20,21] and cell-matrix interactions [22–24]. Furthermore, they can facilitate better screening of nanomedicines [25,26]. 3D *in vitro* models also yield more predictive *in vitro* data and support the reduction of animal studies which are costly and suffering from high failures rates; for all these reasons, 3D *in vitro* models are particularly attractive for screening of clinically relevant properties of nanomedicines [27].

Various platforms have been proposed for generating 3D cell models and for 3D cell cultures, using scaffolds based on different polymers [28], hydrogels [29], microwell arrays [30], hanging drop method [31], and microfluidic devices [32], or combinations thereof [33]. In particular, Sridhar et al. [34] reported a hot-embossed polystyrene-based microwell array in a conventional Petri dish for production of homogenously-sized spheroids, which is rapid and easy to handle while being suitable for *in situ* microscopic examination.

In this study, we developed a 3D spheroid array by co-culturing tumor cells and fibroblasts to mimic tumor stroma *in vitro*, which we subsequently applied for studying nanoparticle penetration. Spheroid arrays were generated in a microwell array which are hot embossed in a polystyrene dish, as reported earlier [34]. Homospheroids (single cell type) and heterospheroids (tumor cells and fibroblasts) were prepared, subsequently characterized for cellular re-organization using confocal laser scanning microscopy as well as for the expression of tumor stromal biomarkers at the transcription and protein levels, and compared to tumor biopsies from patients. To investigate the effect of stroma on nanoparticle penetration in tumors, we incubated homo- and hetero-spheroids with silica nanoparticles of different sizes and surface charges for up to 48 h and examined/quantified their distribution in the spheroids. Finally, we prepared pegylated poly(D,L-lactic-*co*-glycolic acid) (PLGA) nanoparticles which are of high clinical relevance [35], and similarly studied their penetration into homo- and heterospheroids using confocal laser scanning microscopy.

2. Materials and methods

2.1. Materials

Dulbecco's Modified Eagle Medium (DMEM) 4.5 g/l with L-glutamine and RPMI-1640 without L-glutamine, L-glutamine were purchased from PAA/GE Healthcare (Eindhoven, The Netherlands). penicillin/streptomycin, hematoxylin, β-mercaptoethanol and polyvinyl alcohol (PVA, Mw 30,000–70,000) were purchased from Sigma-Aldrich (Zwijndrecht, The Netherlands). Dulbecco's Phosphate Buffered Saline (DPBS) without calcium and magnesium was purchased from Lonza Benelux BV (Breda, The Netherlands). Trypsin-EDTA 0.5% and fetal bovine serum (FBS) were purchased from Life Technologies (Bleiswijk, The Netherlands), together with Cell Trace® Calcein Red-Orange AM and Calcein AM. Pluronic®F-127 was from BASF (USA). Cryomatrix™ was purchased from Thermo Scientific (Cheshire, UK). Target Retrieval Solution at pH 9 was obtained from Dako Agilent (Heverlee, Belgium). VectaMount™ Permanent Mounting Medium was purchased from Vector Laboratories (Peterborough, UK). 3-Amino-9-ethyl-carbazole (AEC Red) was from Invitrogen (Breda, The Netherlands). Aquatex® aqueous mounting medium was purchased from Millipore (USA). iScript™ cDNA Synthesis Kit was purchased from BioRad (Hercules, CA). 2× SensiMix SYBR and Fluorescein Kit was purchased from Bioline (Luckenwalde, Germany). Silica nanoparticles (sicastar®-redF-COOH or sicastar®-redF-NH_2 (size of 30 nm, excitation: 569 nm, emission: 585 nm) and sicastar®-greenF-COOH (size 100 nm, excitation: 485 nm, emission: 510 nm) or sicastar®-redF-NH_2 (size of 70 nm, excitation: 485 nm, emission: 510 nm) were obtained from Micromod Partikeltechnologie GmbH (Rostock, Germany). Uncapped PLGA (lactide/glycolide molar ratio 50:50, IV = 0.4 dl/g) were obtained from Corbion Purac (Amsterdam, The Netherlands). $mPEG_{2000}$-PLGA was synthesized by ring opening polymerization [36]. Ethyl acetate was from VWR chemicals (Amsterdam, The Netherlands). Cyanine-5 amine was from Lumiprobe (Hannover, Germany). MilliQ water was obtained using Millipore Advantage A10 (USA).

2.2. Tissue microarrays (TMAs)

The TMAs of human breast cancer patients were prepared at the pathology lab of LabPON (Hengelo, The Netherlands) which were constructed from biopsies isolated from 11 patients of invasive adenocarcinoma grade 2 to 3 (4 different spots of 2 mm in diameter from each patient). The TMAs were stored at room temperature and subjected to immunohistochemistry staining for activated fibroblast marker (α-SMA and collagen-1α1). Immunohistochemical staining was carried out including standard deparaffinization, through heating to 80 °C in Target Retrieval Solution at pH 9.0 overnight before use, incubation with primary, secondary, and tertiary antibodies and development with DAB (di-aminobenzidine). The TMAs were subsequently counterstained with hematoxylin and mounted with VectaMount™ Permanent Mounting Medium. The TMA slides were scanned using Nanozoomer-RS (Hamamatsu Photonics, Japan). The tissue microarray cores were individually analyzed using NIH Image J software to quantitate the intensity of brown staining from DAB color development for each patient core.

2.3. Cell culture

Mouse 4T1 breast cancer cells, murine NIH3T3 fibroblasts, human pancreatic cancer cell line (Panc-1), and human breast tumor cell line (MDA-MB-231) were obtained from American Type Culture Collection

(ATCC, Rockville, MD). Human primary pancreatic stellate cells (hPSCs) were obtained from ScienCell (Carlsbad, CA) and were cultured in specific medium provided by the manufacturer, supplemented with penicillin/streptomycin. BJ-hTERT foreskin fibroblasts were kindly provided by Prof. Ostman, Karolinska Institute, Stockholm, Sweden. 4T1 and BJ-hTert Fibroblasts were cultured in Roswell Park Memorial Institute (RPMI) 1640 medium, supplemented with 2 mM L-glutamine, 10% fetal bovine serum (FBS) and antibiotics (50 U/ml Penicillin and 50 ng/ml streptomycin. NIH3T3, MDA-MB-231, and Panc-1 cells were cultured in Dulbecco's modified Eagle's medium (DMEM) supplemented with 2 mM L-glutamine, 10% FBS and antibiotics (50 U/ml Penicillin and 50 μg/ml streptomycin). All cells were grown in cell culture treated 75 cm^2 flasks in a humidified incubator at 37 °C with 5% CO_2. Cells were passaged every 3 days and 0.05% trypsin-EDTA in PBS was used for cell detachment.

2.4. 3D-spheroid formation and characterization

2.4.1. 3D-spheroid array formation

Microstamped Petri dishes were produced as previously described by hot embossing microwell arrays (108 wells of 200 μm depth, 400 μm diameter) in commercially available Petri dishes using a home-made set-up [34]. Thereafter and prior to use, the dishes were sterilized in isopropyl alcohol, incubated overnight with a protein repellent coating consisting of 1% w/v Pluronic ® F-127, and washed with PBS before seeding the cells. Cells (2×10^6 cells/dish) were seeded in the microstamped Petri dishes, and centrifuged at 2500 rpm for 5 min to force the cells in the microwells. Culture medium was aspirated, the excess of cells removed and the dishes washed with PBS twice. Fresh 1 ml DMEM was subsequently added and the dishes placed back in the incubator for spheroid formation. Cells were co-cultured at different ratios of 3T3 to 4T1 cells (1:1 and 5:1), and 4T1 or 3T3 homospheroids were used as controls. Human spheroids were generated at ratio 5:1 of BJ hTERT to MDA-MB-231 or hPSC to Panc-1. MDA-MB-231 or Panc-1 homospheroids were generated as controls, respectively. After 48 h, spheroids were used for all experiments.

2.4.2. Characterization of spheroids

The spheroids were characterized for cellular reorganization by labelling 4T1 with Calcein AM (2 μg/ml in culture media, green color) and 3T3 with Cell Trace® Calcein Red-Orange AM (4 μg/ml in culture media, pseudo-color blue) prior to spheroid formation. After 1 h incubation at 37 °C, the medium was removed and cells were washed twice with PBS. Labeled cells were utilized for spheroid formation, as described above. The resulting intact and live spheroids were imaged using confocal laser scanning microscope (Nikon A1R-A1 confocal system, 10× objective) after 24 and 48 h.

2.4.3. Immunostaining of CAF biomarkers

Spheroids grown in microwells were washed with PBS and subsequently embedded in Cryomatrix™. The resulting spheroid array was cut into 8 μm-thick sections and processed for immunostaining. Cryosections were first fixed with acetone at room temperature (RT) for 15 min, rehydrated in PBS and incubated with either mouse anti-α-SMA (Sigma-Aldrich, 1:400), or goat anti-collagen type I (Southern Biotech, 1:100) in PBS for 1 h at RT. Subsequently, sections were washed again in PBS and incubated with secondary antibody–horseradish peroxidase (HRP)-labeled rabbit anti-mouse IgG (DAKO, 1:100) or HRP-labeled goat anti-rabbit IgG (DAKO, 1:100) in PBS for 1 h. Sections were washed again with PBS and finally incubated with a tertiary antibody – HRP-labeled goat anti-rabbit IgG (DAKO, 1:100) or HRP-labeled rabbit anti-goat IgG (DAKO, 1:100) in PBS for 1 h. The peroxidase activity was developed with 3-amino-9-ethyl-carbazole (AEC) in MilliQwater for 20 min. Samples were subsequently counterstained with hematoxylin to visualize cell nuclei, washed in running tapwater for 5 min, and mounted with Aquatex®. Imaging was performed using Nanozoomer-RS. To quantify the staining, single spheroid sections at a 20× magnification were analyzed using ImageJ software (ImageJ, NIH, USA) at a fixed threshold.

2.5. Quantitative real time RT-PCR

Cells grown in 12 well plates (8×10^4 cells/well for 2D samples) or 3D spheroids were harvested after 48 h and lysed with RNA lysis buffer constituted with β-mercaptoethanol to perform quantitative real time RT-PCR analysis for fibrotic parameters (Collagen-1α1 and α-SMA). The total RNA was reverse-transcribed using iScript™ cDNA Synthesis Kit, and real-time PCR reactions were performed using 10 ng of the resulting cDNA, pre-tested gene-specific primer sets, and 2× SensiMix SYBR and Fluorescein Kit according to the manufacturer's instructions. The cycling conditions for the BioRad CFX384 Real-Time PCR detection system were 95 °C for 10 min, 40 cycles of 95 °C for 15 s, 58 °C for 15 s and 72 °C for 15 s. The threshold cycles (Ct) were calculated, the relative gene expression values were normalized to the housekeeping gene GAPDH and fold changes in expression were calculated using the $2^{-\Delta\Delta Ct}$ method. All primers were purchased from Sigma-Genosys (Haverhill, UK). Primer sequences are given in Table 1.

2.6. PLGA nanoparticles preparation and Cy-5 conjugation

PLGA nanoparticles were prepared by the double emulsion solvent evaporation method [37]. Briefly, the internal water phase (100 μl MilliQ water) was emulsified in 1 ml ethyl acetate containing 30% $mPEG_{2000}$-PLGA blended with PLGA (lactide/glycolide molar ratio 50:50, IV = 0.4 dl/g, molecular weight of 44,000 Da), the total polymer concentration being 2.5% w/v. The emulsification was performed in an ice-bath using an ultrasonic homogenizer (Branson Sonifier 250, Branson Ultrasonics Corporation, Danbury, USA) for 1 min at 5% power output. Subsequently, w/o microemulsion was formed which was subsequently emulsified into an external aqueous phase of 2 ml of 2% PVA (w/v) (Mw 30,000–70,000), drop by drop under constant vortexing at maximum speed. The formed water-in-oil-in-water (w/o/w) microemulsion was subsequently sonicated for 2 min at 5% power output. Next, the double emulsion was transferred into 45 ml of 0.3% PVA (w/v) under magnetic stirring, and stirred overnight at RT to let ethyl acetate evaporate and to solidify the emulsified droplets. Particles were isolated by centrifugation for 60 min at 16,000 rpm (Rotor SS-34, Sorvall RC-5C Plus, Kendro Lab, USA), and the supernatant was discarded. Finally, the particles were washed with 30 ml of PBS and water, successively, and lyophilized overnight. Lyophilized PLGA nanoparticles were labeled with Cyanine-5-amine in dry DMF *via* EDC/NHS activation. EDC/NHS mixture in MES Buffer (40 mM) was added to 200 μl PLGA nanoparticles suspension (25 mg/ml) and react for 45 min at RT. The resulting activated PLGA nanoparticles were resuspended in PBS and reacted with 10 μl of Cyanine-5-amine in dry DMF (10 mg/ml) for 2 h at RT. The resulting Cy5-conjugated PLGA nanoparticles (Cy5-PNPs) were purified on an Amicon® column by washing with PBS thrice, resuspended in PBS (25 mg/ml), and stored at 4 °C. The resulting nanoparticles were characterized for size and zeta potential measurements using a Nano ZS Zetasizer (Malvern Instruments, Malvern, UK) at 20 °C. Nanoparticles were suspended in MilliQ® water and their average size and size distribution was determined by dynamic light scattering (DLS) using a Nano ZS Zetasizer. Nanoparticles were suspended in 0.1 mM KCl and injected to a disposable capillary cell DTS 1070 (Malvern Instruments, UK) for zeta potential measurement.

2.7. Penetration study of nanoparticle

2.7.1. Silica nanoparticles

Homo- and heterospheroids grown for 48 h were exposed to silica nanoparticles (Sicastar®-redF-COOH or Sicastar®-redF-NH_2 (size of 30 nm, excitation: 569 nm, emission: 585 nm) and Sicastar®-greenF-

Table 1
Primer sequences.

Target	Forward	Reverse
α-SMA mus	ACTACTGCCGAGCGTGAGAT	CCAATGAAAGATGGCTGGAA
Col-1α1 mus	TGACTGGAAGAGCGGAGAGT	ATCCATCGGTCATGCTCTCT
Periostin mus	ATCCACGGAGAGCCAGTCAT	TGTTTCTCCACCTCCTGTGG
E-Cadherin mus	AACCCAAGCACGTATCAGGG	GAGTGTTGGGGGCATCATCA
FSP-1 mus	CTCTTGGTCTGGTCTCAACGG	TGTCACCCTCTTTGCCTGAG
GAPDH mus	ACAGTCCATGCCATCACTGC	GATCCACGACGGACACATTG

COOH or Sicastar®-redF-NH_2 (size of 100 nm, excitation: 485 nm, emission: 510 nm) for 24 h. Spheroids were incubated with silica nanoparticles in microwelled-Petri dishes at final concentrations of 100 μg/ml in serum-free DMEM medium. Thus, nanoparticles diffuse passively from all directions around the spheroids. After 24 h nanoparticle incubation, spheroids were proceeded for cryoembedding in Cryomatrix®. Cryosections (8 μm-thickness) were collected using Cryotome® FSE (Thermo Fisher Scientific, Cheshire, UK) and allowed to adhere to Superfrost microscopic glass slides (Menzel-Gläser, Braunschweig, Germany). Subsequently, cryosections were air-dried and fixed with acetone at room temperature for 20 min and rehydrated with PBS. Nuclei were stained using DAPI-containing mounting medium. Silica nanoparticle penetration in spheroid was observed by taking fluorescent images of cryosections from central part of spheroids. Cryosections were captured at 20× magnification with fixed exposure time per color using fluorescence microscope (Nikon Eclipse E400, Tokyo, Japan). Subsequently, fluorescent silica nanoparticles penetration was analyzed digitally using NIH ImageJ software.

2.7.2. Cy-5-conjugated PLGA nanoparticles (Cy5-PNPs)

Homospheroids of 4T1 tumor cells and heterospheroids formed with different ratios of 4T1 and 3T3 cells were incubated with 1.25 μg/μl of Cy5-PNPs suspended in serum-free DMEM medium. Spheroids were incubated with Cy5-PNPs in microwelled-Petri dishes in a humidified incubator at 37 °C with 5% CO_2. After exposure to Cy5-PNPs, 3 intact spheroids per time point were washed with PBS and subsequently mounted in PBS for confocal imaging. Confocal images were taken using a confocal laser scanning microscopy (Nikon A1R-A1 confocal system, 10× objective) at 1, 24, and 48 h to observe the penetration of the PLGA nanoparticles into intact and live spheroids. Calcein green fluorescence representing 4T1 tumor cells was excited using 488 nm laser line. Pseudo-color blue of calcein red-orange fluorescence, representing NIH3T3 cells, was visualized with 575 nm laser excitation. Red fluorescence of Cy5 dye, representing PLGA NPs conjugated to Cy5 dye, was excited with 638 nm laser line. Subsequently, Cy5-PNPs penetration were quantified digitally using NIH ImageJ software.

3. Results and discussion

3.1. Human breast tumor stroma pathology

Before designing a tumor stroma-enriched 3D *in vitro* system, it is crucial to characterize the tumor stroma pathology. Therefore, the tumor stroma content and organization in human breast tumor tissues was first studied using a tissue microarray comprised of tumor specimens from 11 patients (4 different spots of 2 mm in diameter from each patient). We performed immunohistochemical staining for α-smooth muscle actin (α-SMA), a marker for cancer-associated fibroblasts (CAFs) [38] and collagen-1 (a common extracellular matrix protein) (Fig. 1). As shown in representative microscopic pictures from different patients (Fig. 1A), the elongated fibrous stroma region (labeled as "S") stained for α-SMA (brown color) reveals the abundance of CAFs, located next to tumor nests (labeled as "T"). Since CAFs are the main cells producing ECM, we also analyzed collagen in a similar way; collagen was found at the α-SMA-positive area within the breast tumor tissue. Furthermore, we quantified the % of tumor stroma within each tumor tissue (Fig. 1B) and found that the α-SMA-positive area (CAF content) lies in a range of 20–55% and collagen-positive area (ECM content) in a range of 40–55%, reflecting the interpatient variability of the stroma content. These data are in line with an earlier study which reported a 31–46% stroma content in breast tumor patients [39].

Furthermore, it is worth noticing that a large number of tumor blood vessels were located in the stromal region (Fig. 1A, indicated as "bv"). These results indicate that nanoparticles extravasating from the bloodstream into the tumor need to cross the stromal barrier to reach the tumor cells. Collectively, these data derived from clinically relevant tissue material show that breast tumors are enriched with stromal tissue which represents a barrier for nanoparticles for reaching the tumor cells.

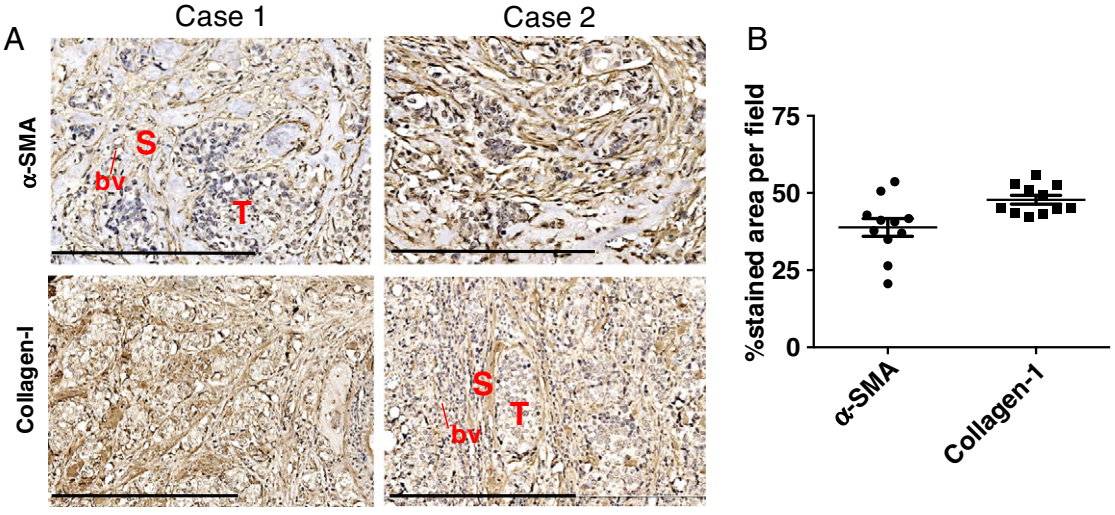

Fig. 1. Microscopic images of immunohistochemical staining in human breast tumor tissues. (A) Representative microscopic images showing α-SMA and collagen-1 staining in human breast cancer sections from two different patient cases. Immunostaining is shown in brown color counterstained with hematoxylin (blue nuclei). "S" and "T" denote stroma and tumor, whereas "bv" indicates blood vessels. Scale bars: 400 μm (B) Semi-quantitative image analysis to measure the % positive (stained) area of α-SMA and collagen-1 immunostaining in tissues using NIH ImageJ software. Each point represents a value for an individual patient. Mean ± SEM, $n = 11$ patients.

3.2. Generation of 3D spheroid arrays in a microwell array platform

To mimic the tumor stroma in 3D culture, heterospheroids composed of 3T3 mouse fibroblasts and 4T1 mouse tumor cells introduced in different ratios (1:1 and 5:1, respectively) were generated, and, as controls, homospheroids from either 4T1 cells or 3T3 cells alone were prepared. Spheroids were produced in a microwell array platform (Fig. 2A, B), which was earlier reported by Sridhar et al. [34]. After seeding, cells self-assembled spontaneously to form spheroids within 48 h, for all cell compositions tested here. Interestingly, 3D *in vitro* cultures involving scaffolds have been reported to take approximately seven days to accurately mimic the *in vivo* tumor phenotypically [25]. At 48 h, shrinkage of the spheroids was observed, which is attributed to establishment of cell-to-cell interactions (Fig. 2C). Macroscopically, no major difference in self-assembling behavior of homospheroids (4T1 or 3T3) and heterospheroids were detected. The average spheroid size after 48 h was found to be 319 ± 18 μm and 320 ± 15 μm for 4T1 and 3T3 homospheroids, respectively, against 365 ± 25 μm and 384 ± 15 μm for 1:1 and 5:1 (3T3:4T1) heterospheroid models, respectively. Noteworthy, the heterospheroid size was larger for relatively higher number of 3T3 fibroblasts, which can be explained by a promotion of tumor cell growth caused by the fibroblasts, as recently suggested [39]. Furthermore, 3T3 homospheroids exhibited the smallest size, which is likely due to the contractile and adhesive property of fibroblasts, allowing them to attach tightly to each other.

3.3. Cellular and molecular characterization of 3D spheroids

Homo- and heterospheroids were characterized in terms of cellular re-organization, expression of stromal markers and stroma content.

3.3.1. Cellular organization

Cellular organization within a spheroid was examined using laser scanning confocal microscopy at 24 and 48 h. Fibroblasts (3T3) and breast cancer cells (4T1) were stained before spheroid formation with Calcein red-orange (pseudocolor; blue) and Calcein-AM (green), respectively (Fig. 3). At a 1:1 (3T3:4T1) ratio, both cell types were distributed homogeneously throughout the spheroids while in the 5:1 spheroids (3T3:4T1), 3T3 cells were more localized to the center, probably due to their higher density, which allowed them to interact together and cluster among themselves. As already mentioned earlier, 3T3 homospheroids shrunk as dense and compact tissues compared to the 4T1 homospheroids and the heterospheroids. Altogether, the fibroblast density influences the cellular organization within the spheroids, which is very likely to impact the biological and physical properties of heterospheroids.

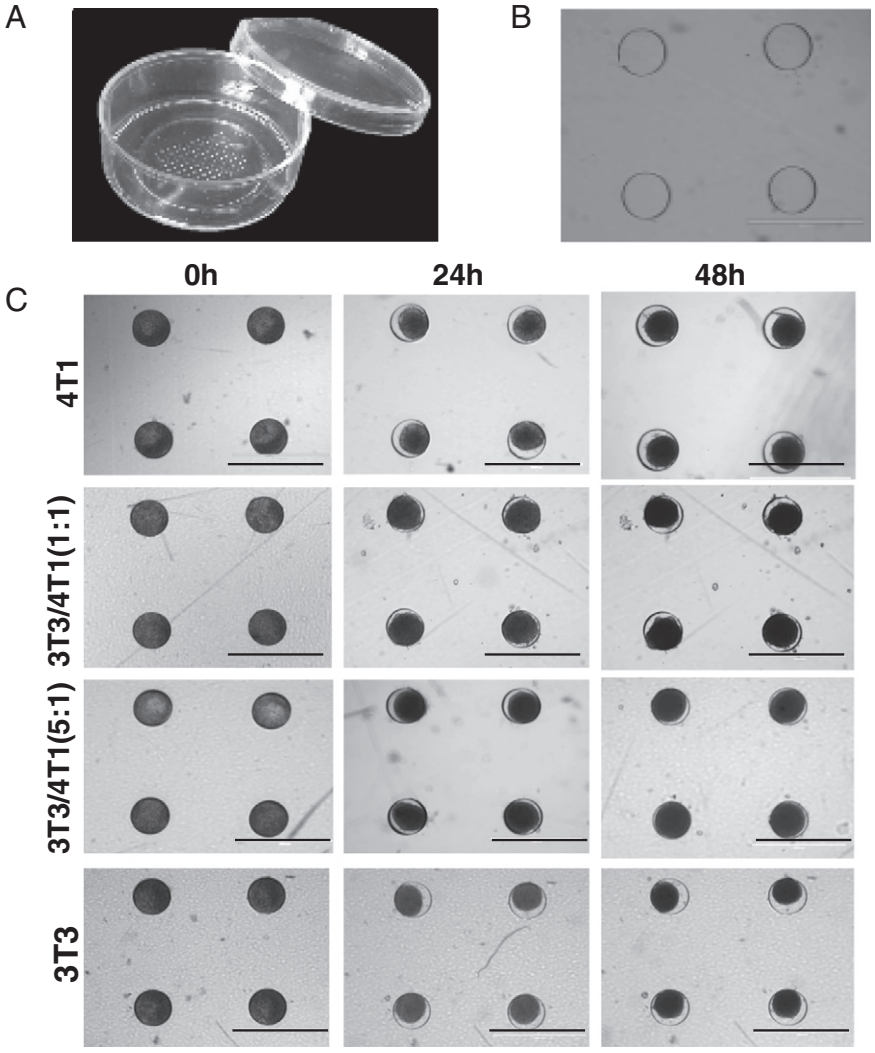

Fig. 2. *In vitro* 3D platform for generating spheroid arrays. (A) A polystyrene Petri dish was stamped using a PDMS master to create a microwell array. (B) Microscopic images showing 4 microwells in a 108 microwell array (200 μm depth, 400 μm diameter). (C) Pictures of 4 independent microwells showing the cell aggregate formation after seeding and at 24 and 48 h. Mouse breast cancer cells (4T1), Mouse fibroblasts (3T3) and their co-culture in 1:1 and 5:1 (3T3: 4T1) ratios cultured in 3D platform. Scale bars: 1000 μm.

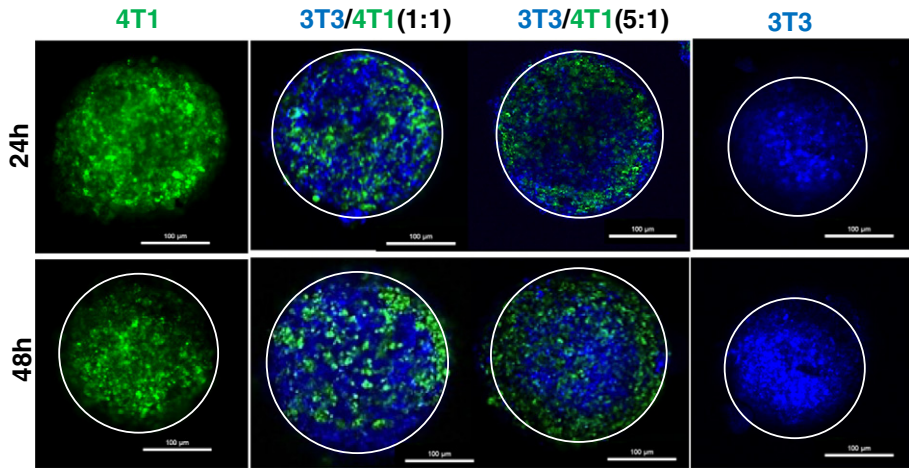

Fig. 3. Confocal fluorescent microscopic images of intact homo- and heterospheroids. 3T3 and 4T1 cells were labeled with calcein red (blue as pseudo-color) and calcein green, respectively, and cultured for 48 h in the microwell array platform. Subsequently, pictures were recorded using confocal microscope to capture the cellular organization of 4T1 (green color) and 3T3 cells (blue as a pseudo-color) after co-culture. Scale bars: 100 μm.

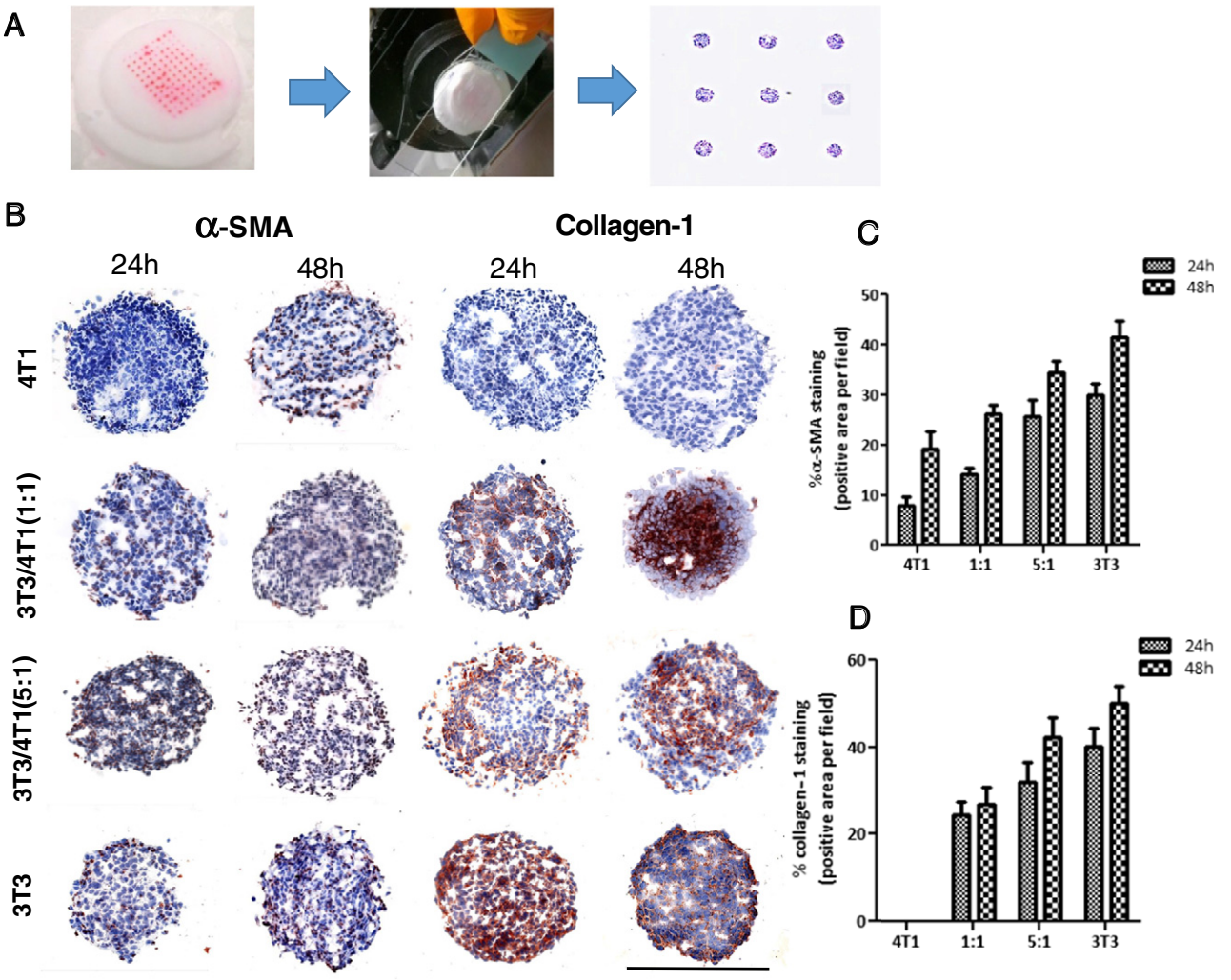

Fig. 4. Spheroid array and stromal markers. (A) Pictures presenting the process used for embedding the spheroid array in Cryomatrix and for preparing cryosections (attached on the glass slide). (B) Microscopic images for the immunostaining of both activated fibroblast marker of alpha-smooth muscle actin (α-SMA) and collagen-1 in mono- and co-culture spheroids. The biomarkers are stained as red, and cell nuclei in blue (hematoxylin) (B) Semi-quantitative image analysis of α-SMA (C) and collagen-1 expression (D). Graphs representing the mean ± SEM of an average of 3–5 spheroids.

3.3.2. Biomarker expression in the spheroid array

To characterize the expression of stromal biomarkers in the various spheroid models, the spheroid arrays from the microwell array platform were isolated and the prepared cryosections were subsequently immunostained (Fig. 4A). Thereafter, the spheroid arrays were scanned with a slide scanner to perform image analysis. The expression of α-SMA (fibroblast marker) and collagen-1α1 (an ECM protein) was examined using immunohistochemical staining (Fig. 4B); 4T1 homospheroids were found to give a low expression of α-SMA at 24 h, which doubled after 48 h, as illustrated in the semi-quantitative image analysis (Fig. 4C). The observed increase in α-SMA expression is likely due to the epithelial-mesenchymal transition (EMT) of the tumor cells [38]. Furthermore, an increase in the fibroblasts-to-tumor cell ratio correlated with a higher expression of α-SMA in heterospheroids at both time points whereas 3T3 homospheroids gave the maximal expression (Fig. 4C). In total, the α-SMA positive area in heterospheroids remained about 30–35% which, interestingly, matches the % stroma found in human breast tumor tissues (Fig. 1B).

Furthermore, 4T1 homospheroids did not express any collagen even after 48 h (Fig. 4B & D), which indicates that the tumor cells undergo EMT but do not attain the capacity to produce collagen. With the increase of the 3T3 content, however, the collagen expression was proportionally enhanced in heterospheroids, attaining a % collagen positive area value of >40% at a 5:1 (3T3:4T1) ratio (Fig. 4D), which again lies in the same range as human breast tumor tissues (Fig. 1C).

3.3.3. Gene expression analyses

Similarly, gene expression analysis was also performed in all spheroid models to quantify the changes in different stromal markers. As immunostaining data indicated that 4T1 tumor cells got activated in a 3D microenvironment (Fig. 4B), the gene expression levels of epithelial and fibroblast markers were compared in 2D and 3D cultures. Interestingly, α-SMA gene expression was found to be significantly enhanced while e-cadherin (epithelial cell marker [38]) gene expression was reduced, confirming that 4T1 tumor cells underwent EMT and differentiated into mesenchymal cells (Fig. 5A). The decrease of e-cadherin

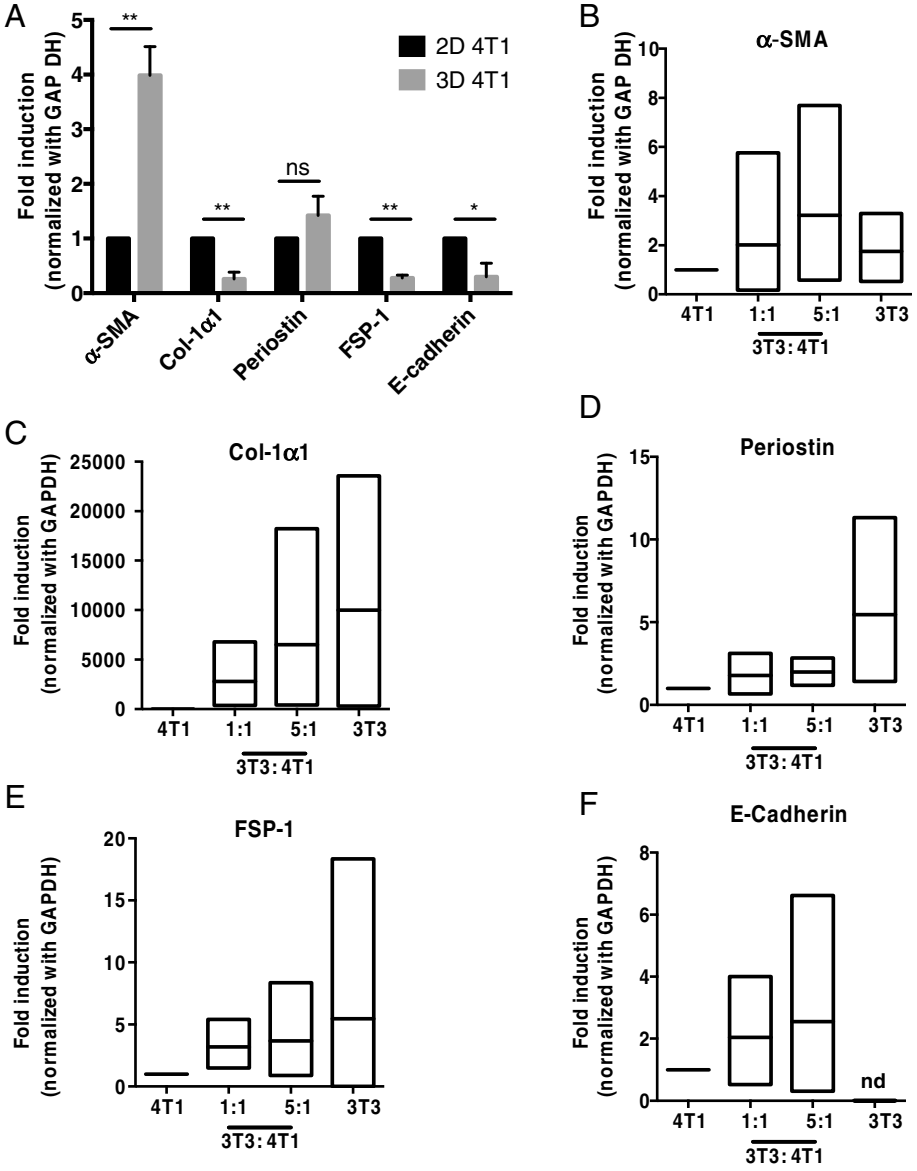

Fig. 5. Gene expression analyses of spheroids. (A) Gene expression (qPCR) analysis for 2D and 3D cultured 4T1 breast tumor cells. Mean ± SEM ($n = 3$–5 samples) $^{*}p < 0.05$, $^{**}p < 0.01$; unpaired two tailed Students' t-test. (B—F) Gene expression analysis for homospheroids (4T1 and 3T3) and heterospheroids (3T3:4T1, 1:1/5:1). Graphs representing the mean of 3–5 spheroids with minimum and maximum limits.

Table 2
Characterization of silica nanoparticles.

Silica nanoparticles	Measured Z-average[a] (d·nm)	PdI[b]	Zeta potential (mV)
RedF 30 nm Sicastar	30 ± 1	0.30 ± 0.01	−40 ± 1
GreenF 100 nm Sicastar	111 ± 1	0.02 ± 0.01	−34 ± 1
RedF 30 nm Sicastar	36 ± 1	0.03 ± 0.01	−23 ± 2
GreenF 70 nm Sicastar	74 ± 1	0.06 ± 0.01	−29 ± 1

[a] Z-average is average size of the intensity weighted mean hydrodynamic size of the ensemble collection of particles measured using dynamic light scattering (DLS; Zetasizer 4000, Malvern Instruments, Malvern, UK).
[b] PdI: polydispersity index.

expression also found in Amman, et al. study [22] in homospheroids of A549 (non-small cell lung cancer cell line, NSCLC) during the course of the cultivation (5 and 10 days), indicating towards a transition to a mesenchymal phenotype.

In addition, it was investigated whether the tumor cells undergoing EMT expressed other markers of CAFs and produced ECM proteins. In line with the immunostaining data, 4T1 tumor cells in 3D culture were found not to fully transform into fibroblasts as they did not express induced FSP-1 and ECM markers (*e.g.*, collagen-1α1 and periostin) (Fig. 5A). Furthermore, heterospheroids with an increasing amount of 3T3 fibroblasts showed higher expression of activated fibroblast markers, including α-SMA, collagen, periostin, and fibroblast-specific protein (FSP-1) (Fig. 5B–E). As expected, spheroids based on 3T3 cells alone exhibited the highest expression for all fibroblast markers. Surprisingly, however, in heterospheroids comprised of 3T3 and 4T1 increased expression of e-cadherin was measured compared to 4T1 homospheroids (Fig. 5F). Amman, et al. study [22] observed a decrease in e-cadherin immunostaining on their heterospheroids, A549 NSCLC cell line with SV-80 lung fibroblast cell line compared to their homospheroids. In contrast, we found an increase of e-cadherin in heterospheroids compared to homospheroids. Since it was observed that 4T1 tumor cells had a significant decrease in e-cadherin levels in 3D culture compared to 2D culture (Fig. 5A), it is likely that in co-culture with fibroblasts 4T1 regained the e-cadherin expression rather than a real enhancement

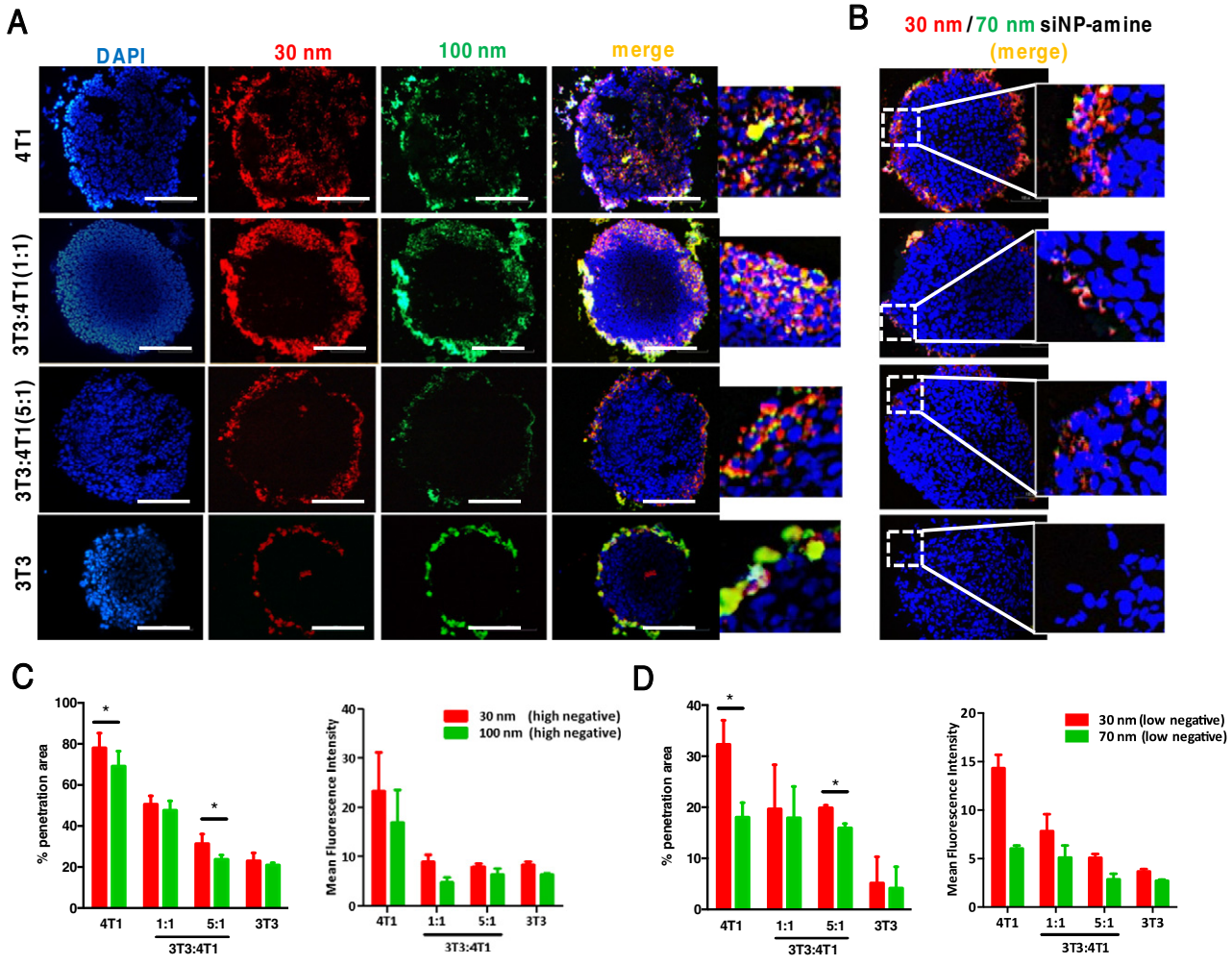

Fig. 6. Penetration of silica nanoparticles into homo- and heterospheroids. (A) Fluorescence microscopy images showing the penetration of silica nanoparticles (30 nm; red fluorescence, 100 nm; green fluorescence, zeta potential −40 mV) into spheroids at 24 h. (B) fluorescence images showing the penetration of silica nanoparticles with low negatively charged fluorescent silica nanoparticles (zeta potential −20 mV) after 24 h. (C and D) Semi-quantitative analysis (% penetration area and mean fluorescent intensity) of silica nanoparticle (high and low negative charge, respectively) penetration using NIH ImageJ software. Data represented as mean ± SEM from 3 to 6 spheroids per condition. Statistic was performed using unpaired *t*-test. $^{*}p < 0.05$.

in heterospheroids. Altogether, these data suggest an active crosstalk between tumor cells and fibroblasts in our spheroids, as revealed through the cellular re-organization and expression of relevant stromal markers, which demonstrates the suitability and versatility of our spheroid array platform to mimic tumor stroma.

3.4. Nanoparticle penetration

The penetration of nanoparticles of different sizes and charges into stroma-rich tumor spheroids was investigated. Specifically, commercially available model silica nanoparticles were first tested, followed by home-made PLGA polymeric nanoparticles, which are of high clinical relevance [35].

3.4.1. Penetration of silica nanoparticles

Differently labeled fluorescent silica nanoparticles (30 nm red color, 100 nm green color; Table 2) were used as model nanoparticles to study the effect of stroma on nanoparticle penetration. Homo- and heteroculture spheroids were incubated with a nanoparticle suspension in serum-free medium for 24 h, and nanoparticle penetration was examined using fluorescent microscopy on cryosections made from the spheroids. Both 30 and 100 nm silica nanoparticles (zeta potential: −40 mV) were detected deep (70–80% positive area) in the 4T1 homospheroids at 24 h (Fig. 6A, C). Interestingly, the addition of fibroblasts to the spheroids (which is associated with an increase of stroma content) inhibited the nanoparticle penetration dramatically, and the lowest penetration was observed in fibroblast homospheroids (Fig. 6A & C). Noticeably, in all cases 30 nm-sized nanoparticles had a better penetration than their 100 nm sized counterparts due to their small size. Interestingly, these data highlight that an increase in stroma content in tissues inhibited nanoparticle penetration proportionally, and that smaller nanoparticles could penetrate deeper in the tissues than large nanoparticles. Furthermore, it would be interesting to investigate how the collagen fiber organization affects the nanoparticle penetration using two photon microscopy.

In a next series of experiments, we examined the influence of the zeta potential on silica nanoparticle penetration. To that end, similar silica nanoparticles but with a less negative zeta potential (−20 *vs.*

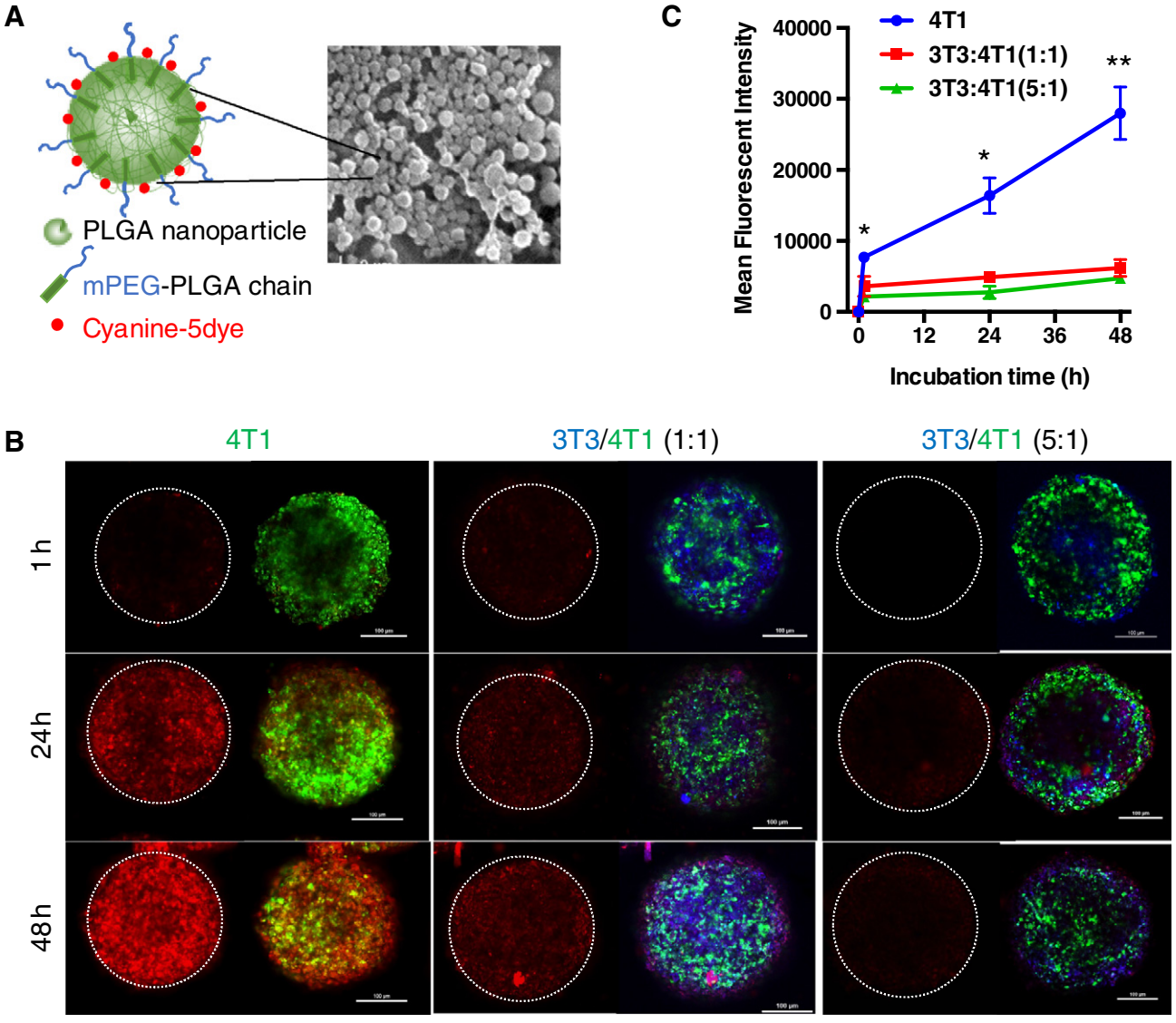

Fig. 7. Penetration of PLGA nanoparticles into homo- and hetero-spheroids. (A) Schematic representation of a PLGA nanoparticle labeled with Cy5 dye (red fluorescence) and scanning electron microscopic image of a PLGA nanoparticle sample; (B) Confocal laser scanning microscopic images of mono- and hetero-spheroids after incubation with Cy-5 PLGA nanoparticles. 4T1 (Calcein green), 3T3 fibroblasts (Calcein red-orange, pseudo-color blue), scale bars: 100 μm; (C) Semi-quantitative analysis of the mean red fluorescence intensity in the homo- and hetero-spheroids. Data represented as mean ± SEM from at least 3 spheroids per condition. Statistic was performed using unpaired *t*-test. $^{*}p < 0.05$, $^{**}p < 0.01$.

−40 mV) were tested under the same conditions. Interestingly, these silica nanoparticles (less negative zeta potential for both 30 and 70 nm sized nanoparticles) penetrated less deeply in all spheroids compared to the more negatively charged nanoparticles (Fig. 6B & D). These results are in good agreement with a previous study by Gao et al. [41] that reported that highly negatively charged nanoparticles interact significantly more with cells compared to nanoparticles with less negative charge. Wilhelm et al. [42] also reported that anionic iron oxide was internalized with high efficiency due to nonspecifically interaction with cell membrane and clustering of the nanoparticles on cationic sites of plasma membrane. These interactions between nanoparticles and cells can facilitate transcellular penetration of nanoparticles through endocytosis and exocytosis (transcytosis) favor deeper penetration as reported before [43]. As before, the penetration of nanoparticles with less negative zeta potential was hindered by the presence of stroma content, and inversely correlated with the amount of stroma

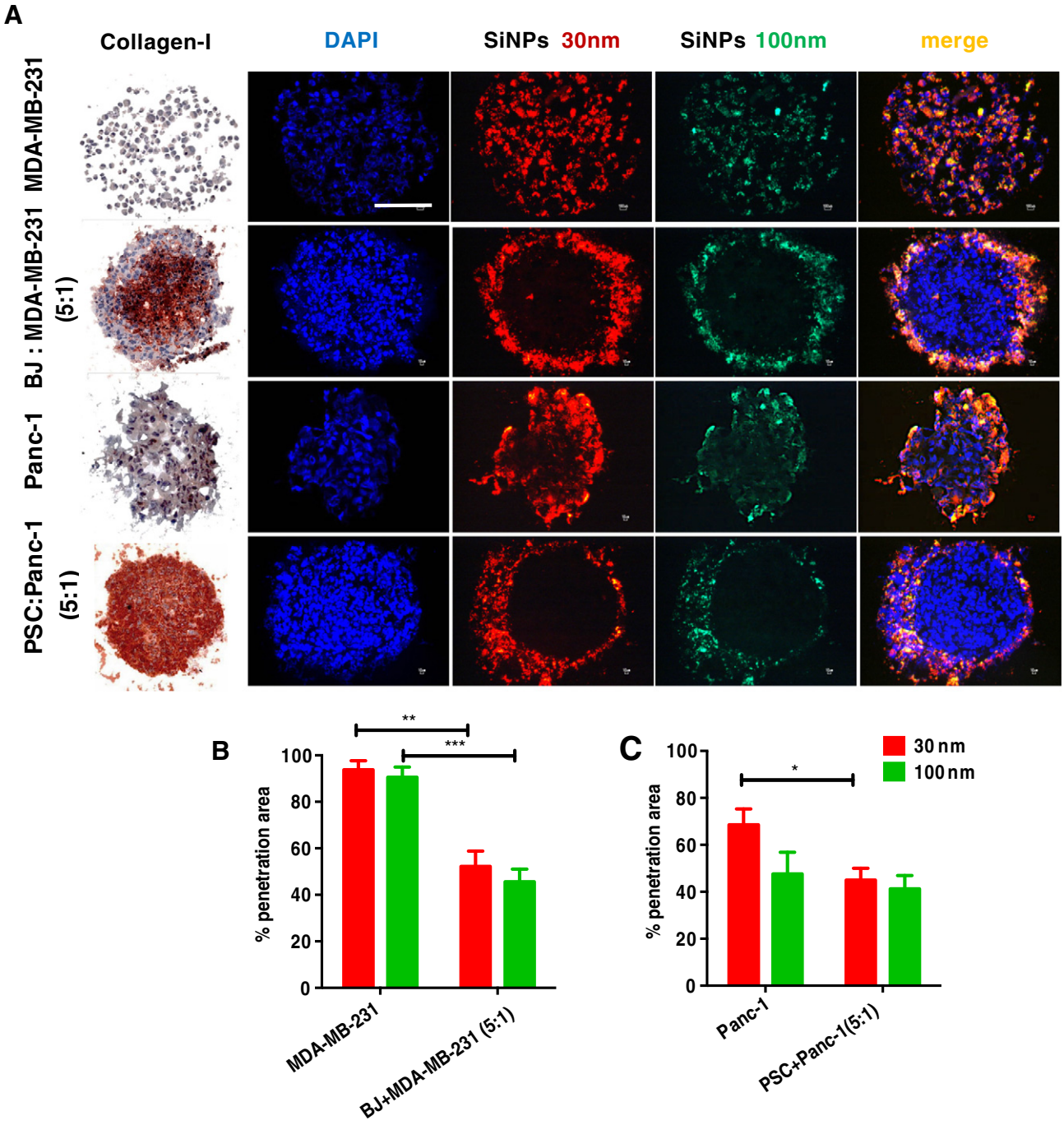

Fig. 8. Characterization of human spheroids and penetration of silica nanoparticles into human spheroids. Homo- and hetero-spheroids of two different human tumor models (breast tumor model using MDA-MB-231 cell line and BJ-hTert human fibroblasts, and human pancreatic tumor model using Panc-1 cell line and primary pancreatic stellate cells (PSC, a CAF precursor cells) were generated and characterized for collagen-1 immunohistochemical stainings. (A) Fluorescence microscopy images showing the penetration of silica nanoparticles (30 nm; red fluorescence, 100 nm; green fluorescence, zeta potential −40 mV) into spheroids at 24 h. Scale bar 100 μm. (B) Semi-quantitative analysis (% penetration area) of high negatively charge silica nanoparticle penetration was performed using NIH ImageJ software. Data represented as mean ± SEM from 3 to 6 spheroids per condition. Statistic was performed using unpaired *t*-test. $^{*}p < 0.05$, $^{**}p < 0.01$, $^{***}p < 0.001$.

(Fig. 6B & D). Yet, and as before, 30 nm-sized silica nanoparticles gave significantly deeper penetration than larger sized (70 nm) nanoparticles. This set of data demonstrate that our heterospheroids are excellent models for studying the penetration of nanoparticles in tumor tissues.

3.4.2. Penetration of Cy5-conjugated PLGA nanoparticles

The spheroid arrays were also applied to study the penetration of pegylated PLGA nanoparticles, which are commonly used nanocarriers for drug delivery [35]. PLGA nanoparticles were prepared with a double emulsion technique, subsequently labeled with Cy5 fluorescent dye and characterized for size (200 ± 4 nm) and zeta potential (-7.1 ± 0.5 mV) (Fig. 7A). Here, laser scanning confocal microscopy was used to monitor the penetration of nanoparticles in intact and live spheroids at different time points. Furthermore, 3T3 fibroblast homospheroids were excluded from this last study as these spheroids without any tumor cell do not mimic a tumor model. As shown in Fig. 7B, Cy5-PLGA nanoparticles slightly penetrated the 4T1 homospheroids within 1 h but did not penetrate the heterospheroids (3T3:4T1 as 1:1 and 5:1). After 24 h, PLGA nanoparticles penetrated through 4T1 homospheroids completely, and the number of nanoparticles found in the spheroids increased substantially at 48 h (Fig. 7C). In contrast, in 3T3/4T1 (both 1:1 and 5:1) heterospheroids, only a little penetration of the PLGA nanoparticles was detected until 48 h. This reduced penetration, especially in stroma containing spheroids, can easily be accounted for by the fact that PLGA nanoparticles were larger in size, than the silica nanoparticles used in this study.

3.4.3. Penetration study in human tumor spheroid models

With regard to better explore the suitability our *in vitro* heterospheroid model mimicking *in vivo* situation, we developed homo- and heterospheroids from human cells from breast tumor and pancreatic tumor. Spheroids were generated from (i) human breast tumor models using MDA-MB-231 human breast tumor cell line and BJ-hTert human fibroblasts, and (ii) human pancreatic tumor model using Panc-1 human pancreatic tumor cell line and primary pancreatic stellate cells (hPSCs, a CAF precursor cells). We established homo- and hetero-spheroids with these cells and characterized for collagen immunohistochemical stainings (Fig. 8A). The collagen-1 expression was strongly present in heterospheroids but remained absent in homospheroids, which is in line of mouse spheroids. Furthermore, we performed silica nanoparticle penetration studies in these homo- and hetero-spheroids (Fig. 8A) and quantified the penetration as %penetration area (Fig. 8B). Similar to the data from mouse spheroid model, the homospheroids comprised of either human breast and pancreatic tumor cells had a deeper penetration of both 30 and 100 nm silica nanoparticles compared to the stroma-containing heterospheroids. Therefore, we conclude that nanoparticle penetration is strongly dependent on the presence of fibroblasts and fibroblast-secreted ECM. Yet, the human spheroid models represent a great tool to study the impact of the clinical-relevant samples.

4. Conclusion

We have successfully developed a 3D spheroid platform to mimic tumor stroma, utilizing tumor cells and fibroblasts showing typical stroma features in terms of stroma content and markers in human breast tumor samples. This 3D model might be applicable to study the tumor-stroma interaction, antitumor effects of drug molecules and nanomedicines, and diffusion/penetration properties of drug-loaded nanomedicines. The presented data obtained in our 3D *in vitro* model confirm that stroma is a barrier for nanoparticle penetration and that the model can be applied to study the tumor penetration properties of nanomedicines.

Acknowledgements

This study was funded by Indonesian Directorate General of Higher Education Scholarships (DIKTI, Jakarta) and Swedish Research Council grant (K7/60501283, JP). (Applied Microfluidics for BioEngineering Research, MIRA Institute, University of Twente, Enschede, The Netherlands) is kindly acknowledged for the support of his technical help in making stamped petri dishes.

References

[1] H. Maeda, J. Wu, T. Saw, Y. Matsumura, K. Horic, Tumor vascular permeability and the EPR effect in macromolecular therapeutics: a review, J. Control. Release 65 (2000) 271–284.
[2] H. Maeda, Macromolecular therapeutics in cancer treatment: the EPR effect and beyond, J. Control. Release 164 (2012) 138–144.
[3] B. Gupta, T.S. Levchenko, V.P. Torchilin, Intracellular delivery of large molecules and small particles by cell-penetrating proteins and peptides, Adv. Drug Deliv. Rev. 57 (2005) 637–651.
[4] Y.H. Bae, K. Park, Targeted drug delivery to tumors: myths, reality and possibility, J. Control. Release 153 (2011) 198–205.
[5] T. Lammers, S. Aime, W.E. Hennink, G. Storm, F. Kiessling, Drug targeting to tumors: principal, pitfalls, and (pre-)-clinical progress, J. Control. Release 161 (2012) 175–187.
[6] F. Danhier, O. Feron, V. Préat, To exploit the tumor microenvironment: passive and active tumor targeting of nanocarriers for anti-cancer drug delivery, J. Control. Release 148 (2010) 135–146.
[7] N. Bertrand, J. Leroux, The journey of a drug-carrier in the body: an anatomo-physiological perspective, J. Control. Release 161 (2012) 152–163.
[8] M.J. Ernsting, M. Murakami, A. Roya, S. Li, Factors controlling the pharmacokinetics, biodistribution and intratumoral penetration of nanoparticles, J. Control. Release 172 (2013) 782–794.
[9] A. Wicki, D. Witzigmann, V. Balasubramanian, J. Huwyler, Nanomedicine in cancer therapy: challenges, opportunities, and clinical applications, J. Control. Release 200 (2015) 138–157.
[10] S. Acharya, S.K. Sahoo, PLGA nanoparticles containing various anticancer agents and tumour delivery by EPR effect, Adv. Drug Deliv. Rev. 63 (2011) 170–183.
[11] R.K. Jain, T. Stylianopoulos, Delivering nanomedicine to solid tumors, Nat. Rev. Clin. Oncol. 7 (2010) 653–664.
[12] R.K. Jain, Normalizing tumor microenvironment to treat cancer: bench to bedside to biomarkers, J. Clin. Oncol. 31 (2013) 2205–2219.
[13] Z. Popovic, W. Liu, V.P. Chauhan, J. Li, C. Wong, A.B. Greytak, N. Insin, D.G. Nocera, D. Fukumura, R.K. Jain, M.G. Bawendi, Angew. Chem. Int. Ed. Eng. 49 (2010) 8649–8652.
[14] H. Cabral, Y. Matsumoto, K. Mizuno, Q. Chen, M. Murakami, cM. Kimura, Y. Terada, M.R. Kano, K. Miyazono, M. Uesaka, N. Nishiyama, K. Kataoka, Accumulation of sub-100 nm polymeric micelles in poorly permeable tumours depends on size, Nat. Nanotechnol. 6 (2011) 815–823.
[15] A. Albanese, A.K. Lam, E.A. Sykes, J.V. Rocheleau, W.C.W. Chan, Tumour-on-a-chip provides an optical window into nanoparticle tissue transport, Nature C Nat. Commun. 4 (2013) 1–8.
[16] H. Fang, Y.A. DeClerck, Targeting the tumor microenvironment: from understanding pathways to effective clinical trials, Cancer Res. 73 (2013) 4965–4977.
[17] D. Öhlund, E. Elyada, D. Tuveson, Fibroblast heterogeneity in the cancer wound, J. Exp. Med. 211 (2014) 1503–1523.
[18] J. Zhang, J. Liu, Tumor stroma as targets for cancer therapy, Pharmacol. Ther. 137 (2013) 200–215.
[19] J. Prakash, Cancer-associated fibroblasts: perspectives in cancer therapy, Trends in Cancer 2 (2016) 277–279.
[20] A. Ivascu, M. Kubbies, Diversity of cell-mediated adhesions in breast cancer spheroids, Int. J. Oncol. 31 (2007) 1403–1413.
[21] L.B. Weiswald, J.M. Guinebretière, S. Richon, D. Bellet, B. Saubamea, V. Dangles-Marie, In situ protein expression in tumour spheres: development of an immunostaining protocol for confocal microscopy, BMC Cancer 10 (2010) 106–116.
[22] A. Amann, M. Zwierzina, G. Gamerith, M. Bitsche, J.M. Huber, G.F. Vogel, M. Blumer, S. Koeck, E.J. Pechriggl, J.M. Kelm, W. Hilbe, H. Zwierzina, Development of an innovative 3D cell culture system to study tumour - stroma interactions in non-small cell lung cancer cells, PLoS ONE 9 (2014), e92511http://dx.doi.org/10.1371/journal.pone.0092511.
[23] W.N. Brennen, D.M. Rosen, H. Wang, J.T. Isaacs, S.R. Denmeade, Targeting carcinoma-associated fibroblasts within the tumor stroma with a fibroblast activation protein-activated prodrug, J. Natl. Cancer Inst. 104 (2012) 1320–1334.
[24] D. Rama-Esendagli, G. Esendagli, G. Yilmaz, D. Guc, Spheroid formation and invasion capacity are differentially influenced by co-cultures of fibroblast and macrophage cells in breast cancer, Mol. Biol. Rep. 41 (2014) 2885–2892.
[25] H. Jaganathan, J. Gage, F. Leonard, S. Srinivasan, G.R. Souza, B. Dave, B. Godina, Three-dimensional in vitro co-culture model of breast tumor using magnetic levitation, Sci. Rep. 4 (2014) 6468, http://dx.doi.org/10.1038/srep06468.
[26] Y. Luo, C. Wang, M. Hossain, Y. Qiao, L. Ma, J. An, M. Su, Three-dimensional microtissue assay for high-throughput cytotoxicity of nanoparticles, Anal. Chem. 84 (2012) 6731–6738.
[27] G. Mehta, A.Y. Hsiao, M. Ingram, G.D. Luker, S. Takayama, Opportunities and challenges for use of tumor spheroids as models to test drug delivery and efficacy, J. Control. Release 164 (2012) 192–204.
[28] J.L. Horning, S.K. Sahoo, S. Vijayaraghavalu, S. Dimitrijevic, J.K. Vasir, T.K. Jain, A.K. Panda, V. Labhasetwar, 3-D tumor model for in vitro evaluation of anticancer drugs, Mol. Pharm. 5 (2009) 849–862.

[29] J. Fukuda, K. Nakazawa, Hepatocyte spheroid arrays inside microwells connected with microchannels, Biomicrofluidics 5 (2011) 22205, http://dx.doi.org/10.1063/1.3576905.
[30] N.C. Rivron, E.J. Vrij, J. Rouwkema, S. Le Gac, A. van den Berg, R. Truckenmüller, C.A. van Blitterswijk, Tissue deformation spatially modulates VEGF signaling and angiogenesis, PNAS 109 (2012) 6881–6891.
[31] J.M. Kelm, N.E. Timmins, C.J. Brown, M. Fussenegger, L.K. Nielsen, Method for generation of homogeneous multicellular tumor spheroids applicable to a wide variety of cell types, Biotechnol. Bioeng. 83 (2003) 173–180.
[32] Y.S. Torisawa, B.H. Chueh, D. Huh, P. Ramamurthy, T.M. Roth, K.F. Barald, S. Takayama, Efficient formation of uniform-sized embryoid bodies using a compartmentalized microchannel device, Lab Chip 7 (2007) 770–776.
[33] O. Frey, P.M. Misun, D.A. Fluri, J.G. Hengstler, A. Hierlemann, Reconfigurable microfluidic hanging drop network for multi-tissue interaction and analysis, Nat. Commun. 5 (2014) 4250.
[34] A. Sridhar, H.L. de Boer, A. van den Berg, S. Le Gac, Microstamped Petri dishes for scanning electrochemical microscopy analysis of arrays of microtissues, PLoS One 9 (2014) 93618, http://dx.doi.org/10.1371/journal.pone.0093618.
[35] F. Danhier, N. Lecouturier, B. Vroman, C. Jérôme, J. Marchand-Brynaert, O. Feron, V. Préat, PLGA-based nanoparticles: an overview of biomedical applications, J. Control. Release 161 (2012) 505–522.
[36] N. Samadi, M.J. van Steenbergen, J.B. vanden Dikkenberg, T. Vermonden, C.F. van Nostrum, M. Amidi, W.E. Hennink, Nanoparticles based on hydrophilic polyester with a sheddable PEG coating for protein delivery, Pharm. Res. 31 (2014) 2593–2604.
[37] N. Samadi, A. Abbadessa, A. Di Stefano, C.F. van Nostrum, T. Vermonden, S. Rahimian, E.A. Teunissen, M.J. van Steenbergen, M. Amidi, W.E. Hennink, The effect of lauryl capping group on protein release and degradation of poly(D,L-lactic-*co*-glycolic acid) particles, J. Control. Release 172 (2013) 436–443.
[38] S. Lamouille, J. Xu, R. Derynck, Molecular mechanisms of epithelial–mesenchymal transition, Nat. Rev. Mol. Cell Biol. 15 (2014) 178–196.
[39] C.L. Downey, H.H. Thygesen, N. Sharma, A.M. Shaaban, Prognostic significance of tumour stroma ratio in inflammatory breast cancer, Springerplus 4 (2015) 68–71.
[41] Y. Gao, M. Li, B. Chen, Z. Shen, P. Guo, M.G. Wientjes, J.L. Au, Predictive models of diffusive nanoparticle transport in 3-dimensional tumor cell spheroids, J. AAPS 15 (2013) 816–831.
[42] C. Wilhelma, C. Billoteya, J. Roger, J.N. Pons, J.C. Bacria, F. Gazeau, Intracellular uptake of anionic superparamagnetic nanoparticles as a function of their surface coating, Biomaterials 24 (2003) 1001–1011.
[43] H. Lu, R.H. Utama, U. Kitiyotsawat, K. Babiuch, Y. Jiang, M.H. Stenzel, Enhanced transcellular penetration and drug delivery by crosslinked polymeric micelles into pancreatic multicellular tumor spheroids, Biomater. Sci. 3 (2015) 1085–1095.